SEARCH FOR RESONANT DOUBLE HIGGS PRODUCTION WITH BBZZ DECAYS IN THE $b\bar{b}\ell\ell\nu\bar{\nu}$ FINAL STATE IN pp COLLISIONS AT $\sqrt{s} = 13$ TeV

by

Rami Kamalieddin

A DISSERTATION

Presented to the Faculty of

The Graduate College at the University of Nebraska

In Partial Fulfilment of Requirements

For the Degree of Doctor of Philosophy

Major: Physics and Astronomy

Under the Supervision of Professor Ilya Kravchenko

Lincoln, Nebraska

May, 2019

SEARCH FOR RESONANT DOUBLE HIGGS PRODUCTION WITH BBZZ DECAYS IN THE $b\bar{b}\ell\ell\nu\bar{\nu}$ FINAL STATE IN pp COLLISIONS AT $\sqrt{s} = 13$ TeV

Rami Kamalieddin, Ph.D.

University of Nebraska, 2019

Advisers: Ilya Kravchenko

Since the discovery of the Higgs boson in 2012 by the A Toroidal LHC ApparatuS (ATLAS) and The Compact Muon Solenoid (CMS), most of the quantum mechanical properties that describe the long-awaited Higgs boson have been measured. Due to an impeccable work of the LHC, dozens of fb^{-1} of data have been delivered to both experiments. Finally, it became possible for analyses that have a very low cross section to observe rare decay modes of the Higgs boson, as was done successfully recently in ttH and VHbb channels. The only untouched territory is a double Higgs boson production. Data will not help us much either at the HL-LHC, the process will remain unseen even in the most optimistic scenarios, so one has to rely solely on new reconstruction methods as well as new analysis techniques. This thesis is addressing both goals. I have been blessed by an opportunity to work in the CMS electron identification group, where we have developed new electron identification algorithms. The majority of this thesis, however, will be devoted to the second goal of HL-LHC. We establish the techniques for the first ever analysis at the LHC that searches for the double Higgs production mediated by a heavy narrow-width resonance in the $b\bar{b}ZZ$ channel: $X \to HH \to b\bar{b}ZZ^* \to b\bar{b}\ell\ell\nu\bar{\nu}$. The analysis searches for a resonant production of a Higgs boson pair in the range of masses of the resonant parent particle from 250 to 1000 GeV. Both spin scenarios of the resonance are considered: spin 0 (later called "graviton") and spin 2 (later called "radion"). In the absence of the

evidence of the resonant double Higgs boson production from the previous searches, we set upper confidence limits. When combined with other search channels, this analysis will contribute to the discovery of the double Higgs production and we would be able to finally probe the Higgs boson potential using its self-coupling.

"... a place for a smart quote!"

Lenin, 1922.

ACKNOWLEDGMENTS

This will be a longggggg list!

Table of Contents

List of Figures

List of Tables

CHAPTER *1*

LHC and the CMS experiment

1.1 Introduction

Large Hadron Collider (LHC) is the most powerful particle accelerator that has ever been built. It is located at the border of the France and Switzerland, reutilising the tunnel used previously by the Large Electron Positron collider. The whole LHC story begins in 1977, when CERN director general Sir John Adams suggested that LEP tunnel can be reused to accommodate the future hadron collider of more than 3 TeV energies **??**. At the 1984 ECFA-CERN workshop on a "Large Hadron Collider in the LEP Tunnel" **??**, the plans for LHC were stated, where the primary ones were the BEH mechanism, Higgs boson, and the origin of masses of W and Z bosons". The parameters of the LHC were very ambitious, the centre-of-mass energy of 10 to 20 TeV, and a target luminosity of $10^{33-34}\frac{1}{cm^2 s}$. Luminosity is the coefficient which refers the cross section of the event under study to the number of events that will be generated in the LHC collision: $N_{events} = L\sigma_{event}$. Luminosity is the parameter control by the machine and for Gaussian beams **??** can be written as:

$L = \frac{N_b^2 n_b f_{rev} \gamma_r}{4\pi\varepsilon_n \beta^\star} F$

where N_b is the number of particle in the colliding bunch, n_b is the number of colliding bunches in the beam, f_{rev} is the revolution frequency, γ_r is the relativistic factor, ε_n is the normalised transverse beam emittance, $\beta^\star$ is the beta function at the collision point, and F is the factor related to the crossing angle at the interaction point (IP). The luminosity is not constant and decays with time due to the degradation of the initial circulating beams. Decay time is approximately 45 h with 29 h to reach $1/e$ level. Adding contribution from the intrabeam scattering, scattering on the residual gas, etc, the final luminosity lifetime is about 15 h. Another useful variation of the luminosity parameter is an integrated luminosity. Integrating over the yield of a single run we get:

$L_{int} = L_0 \tau_L \left[1 - e^{\frac{-T_{run}}{\tau_L}}\right]$, where L_0 is the initial luminosity, T_L is the total length of the run, and τ_L is the luminosity lifetime. The optimum runtime thus is either 5.5 or 12 hours, which potentially leads to $80 - 120/fb$ of data with barn b denoting a unit area of 10^{28} m^2.

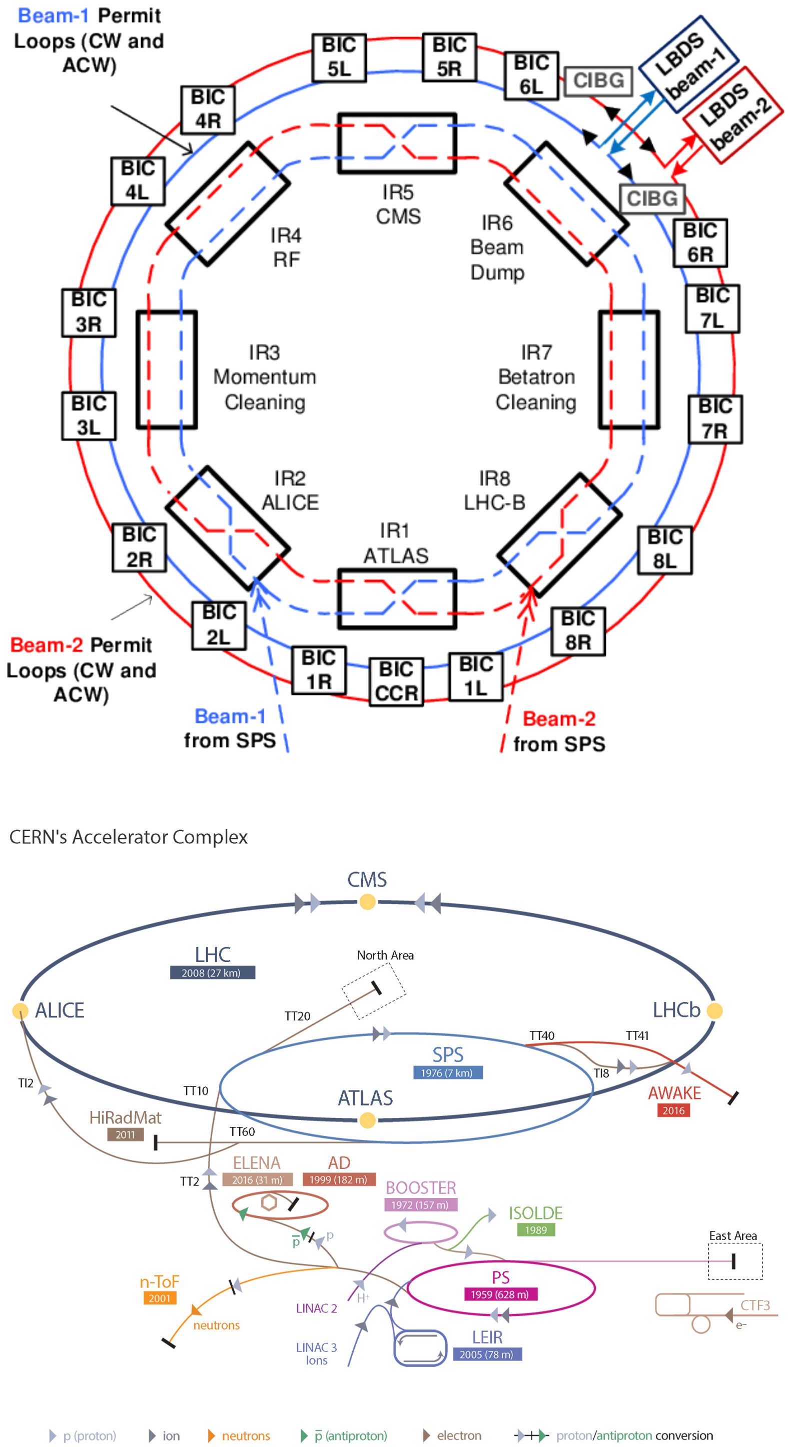

Figure 1.1: Schematic layout of the LHC .

The first LHC budget plan was approved in 1996 and the final cost sum was completed in 2008. And as we already mentioned, the Higgs discovery happened in 2012, quite fast for such a huge project!

1.2 The LHC

With 27 km of circumference, the LHC is currently the most powerful circular accelerator in the world. It is installed in the same tunnel where the Large Electron-Positron (LEP) collider was located, taking advantage of the existing infrastructure. The LHC is part of the CERN's accelerator complex composed of several successive accelerating stages before the particles are injected into the LHC ring where they reach their maximum energy (see Figure 1.2).

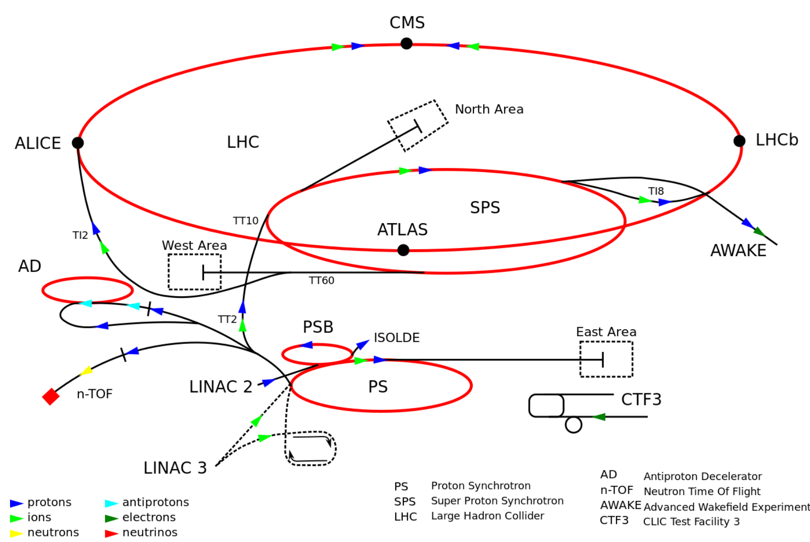

Figure 1.2: CERN accelerator complex. Blue arrows show the path followed by protons along the acceleration process [**?**].

The LHC runs in three collision modes depending on the particles being accelerated

- Proton-Proton collisions (pp) for multiple physics experiments.

- Lead-Lead collisions (Pb-Pb) for heavy ion experiments.
- Proton-Lead collisions (p-Pb) for quark-gluon plasma experiments.

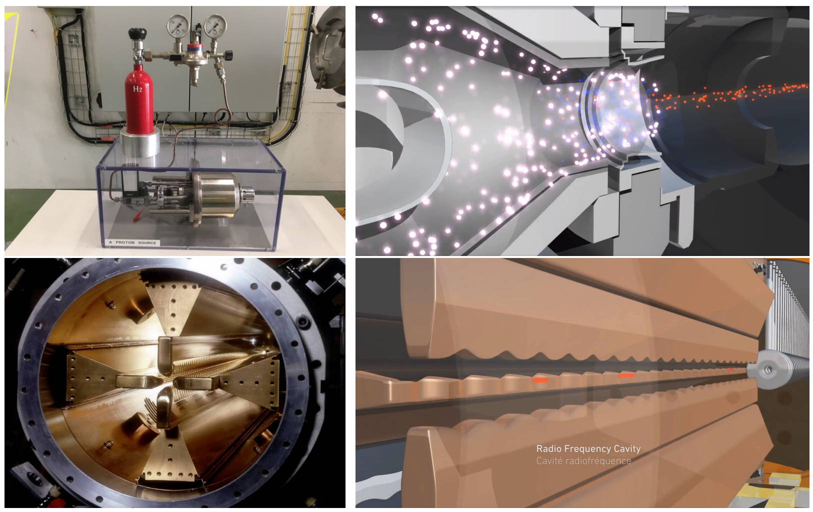

Figure 1.3: LHC protons source and the first acceleration stage. Top: the bottle contains hydrogen gas which is injected into the metal cylinder (white dots) to be broken down into electrons (blue dots) and protons (red dots); Bottom: the obtained protons are directed towards the radio frequency quadrupole which perform the first acceleration, focus the beam and create the bunches of protons. Letf images are real pictures while right images are drawings [**?**, **?**].

In this thesis only *pp* collisions will be considered.

Collection of protons starts with hydrogen atoms taken from a bottle, containing hydrogen gas, and injecting them in a metal cylinder; hydrogen atoms are broken down into electrons and protons by an intense electric field (see Figure 1.3 top). The resulting protons leave the metal cylinder towards a radio frequency quadrupole (RFQ) that focus the beam, accelerates the protons and creates the packets of protons called bunches. In the RFQ, an electric field is generated by a RF wave at a frequency that matches the resonance frequency of the cavity where the electrodes are contained. The beam of protons traveling on the RFQ axis experiences an alternating electric field gradient that generates the focusing forces.

In order to accelerate the protons, a longitudinal time-varying electric field component is added to the system; it is done by giving the electrodes a sine-like profile as shown in Figure 1.3 bottom. By matching the speed and phase of the protons with the longitudinal electric field the bunching is performed; protons synchronized with the RFQ (synchronous protons) do not feel an accelerating force, but those protons in the beam that have more (or less) energy than the synchronous proton (asynchronous protons) will feel a decelerating (accelerating) force; therefore, asynchronous protons will oscillate around the synchronous ones forming bunches of protons [?]. From the RFQ protons emerge with energy 750 keV in bunches of about 1.15×10^{11} protons [?].

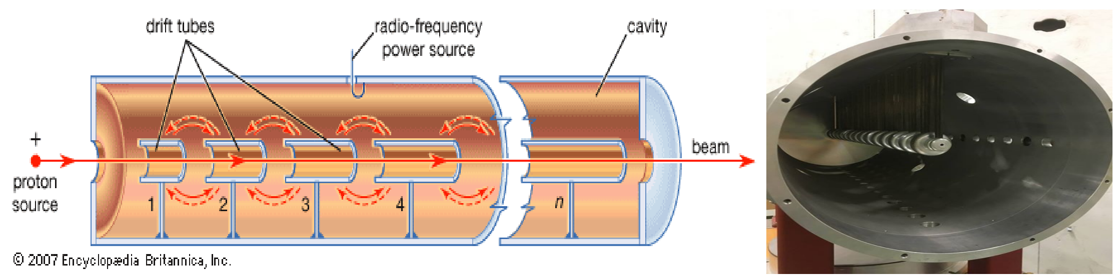

Figure 1.4: Left: drawing of the LINAC2 accelerating system at CERN. Electric fields generated by radio frequency (RF) create acceleration and deceleration zones inside the cavity; deceleration zones are blocked by drift tubes where quadrupole magnets focus the proton beam. Right: picture of a real RF cavity [?].

Proton bunches coming from the RFQ go to the linear accelerator 2 (LINAC2) where they are accelerated to reach 50 MeV energy. In the LINAC2 stage, acceleration is performed using electric fields generated by radio frequency which create zones of acceleration and deceleration as shown in Figure 1.4. In the deceleration zones, the electric field is blocked using drift tubes where protons are free to drift while quadrupole magnets focus the beam.

The beam coming from LINAC2 is injected into the proton synchrotron booster (PSB) to reach 1.4 GeV in energy. The next acceleration is provided at the proton synchrotron (PS) up to 26 GeV, followed by the injection into the super proton synchrotron (SPS) where protons are accelerated to 450 GeV. Finally, protons are injected into the LHC where they are accelerated to the target energy of 6.5 TeV.

PSB, PS, SPS and LHC accelerate protons using the same RF acceleration technique described before.

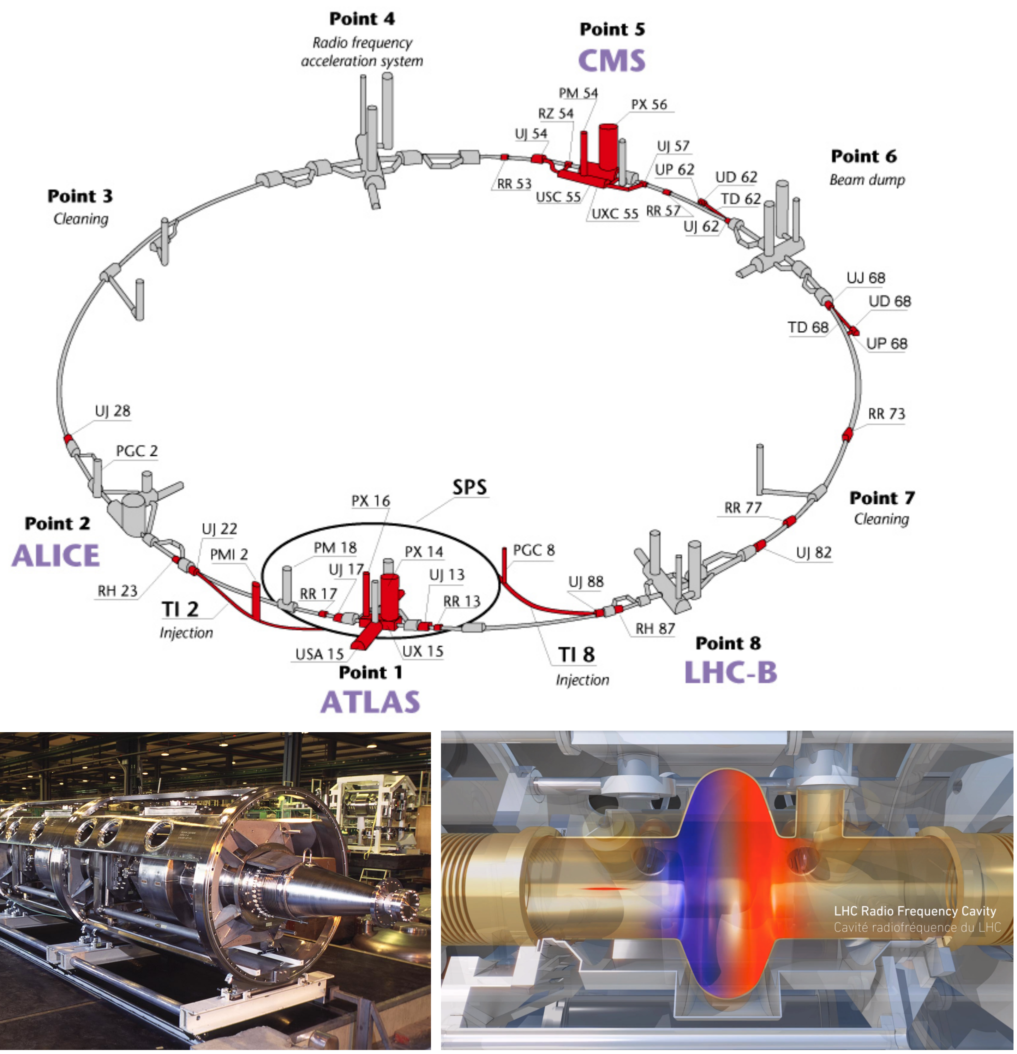

Figure 1.5: Top: LHC layout. The red zones indicate the infrastructure additions to the LEP installations, built to accommodate the ATLAS and CMS experiments which exceed the size of the former experiments located there [**?**]. Bottom: LHC RF cavities. A module (left picture) accommodates 4 cavities, each like the one in the right drawing, that accelerate protons and preserve the bunch structure of the beam. The color gradient pattern represents the strenght of the electric field inside the cavity; red zone corresponds to the maximum of the oscillation electric field while the blue zore corresponds to the minimum. [**?**, **?**]

The LHC has a system of 16 RF cavities located in the so-called point 4, as shown in Figure 1.5 top, tuned at a frequency of 400 MHz. The bottom side of Figure 1.5 shows a picture of a RF module composed of 4 RF cavities working in a superconducting state at 4.5 K; also, a representation of the accelerating electric field that accelerates the protons in the bunch is shown. The maximum of the oscillating electric field (red region) picks the proton bunches at the the entrance of the cavity and keeps accelerating them through the whole cavity. The protons are carefully timed so that in addition to the acceleration effect the bunch structure of the beam is preserved.

While protons are accelerated in one section of the LHC ring, where the RF cavities are located, in the rest of their path they have to be kept in the curved trajectory defined by the LHC ring. Technically, LHC is not a perfect circle; RF, injection, beam dumping, beam cleaning and sections before and after the experimental points where protons collide are all straight sections. In total, there are 8 arcs 2.45 km long each and 8 straight sections 545 m long each. In order to curve the proton's trajectory in the arc sections, superconducting dipole magnets are used.

Inside the LHC ring, there are two proton beams traveling in opposite directions in two separated beam pipes; the beam pipes are kept at ultra-high vacuum ($\sim 10^{-9}$Pa) to ensure that there are no particles that interact with the proton beams. The superconducting dipole magnets used in LHC are made of a NbTi alloy, capable of transporting currents of about 12000 A when cooled at a temperature below 2K using liquid helium (see Figure 1.6).

Protons in the arc sections of LHC feel a centripetal force exerted by the dipole magnets; the magnitude of magnetic field needed to keep the protons in the LHC

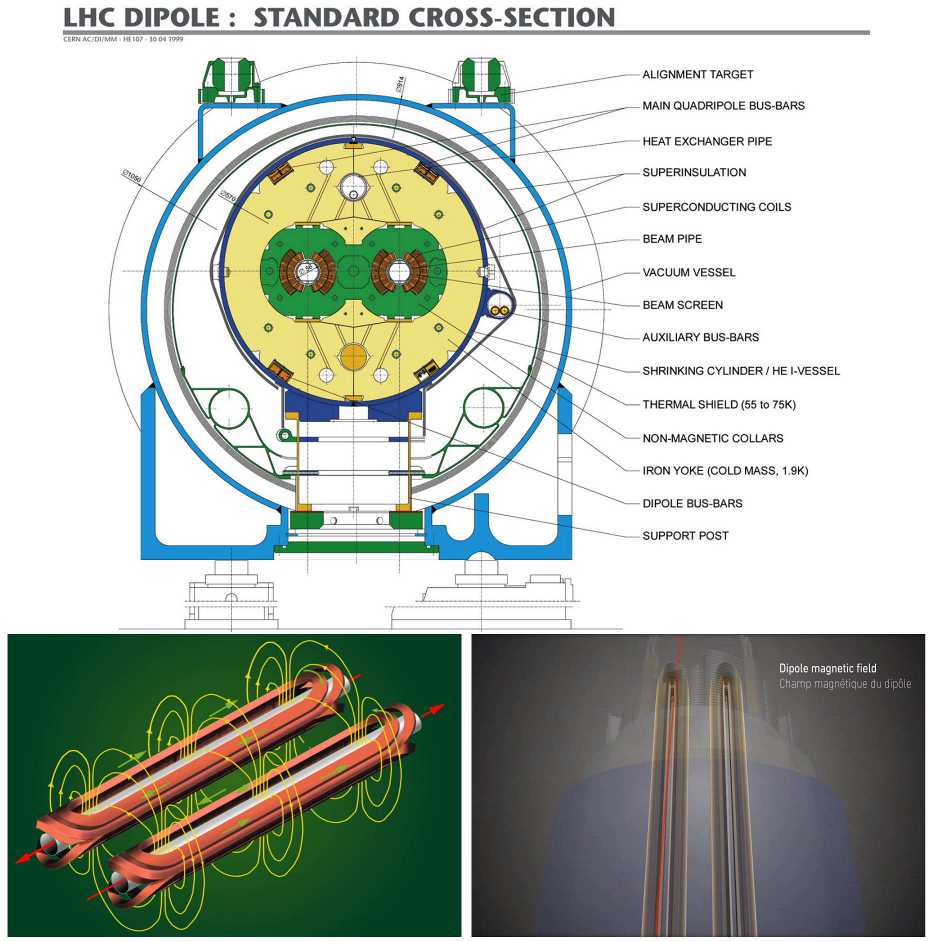

Figure 1.6: Top: LHC dipole magnet transverse view; cooling, shielding and mechanical support are indicated. Bottom left: Magnetic field generated by the dipole magnets; note that the direction of the field inside one beam pipe is opposite with respect to the other beam pipe which guarantee that both proton beams are curved in the same direction towards the center of the ring. The effect of the dipole magnetic field on the proton beam is represented on the bottom right side [**?**, **?**, **?**].

curved trayectory can be found by considering the Loretz force

$$\frac{d\mathbf{p}}{dt} = q\mathbf{v} \times \mathbf{B}. \tag{1.1}$$

Solving for $\mathbf{p}$, it is found that

$$\frac{p}{q} = Br \tag{1.2}$$

where p is the proton's momentum (7 TeV/c), q is the proton's charge and r is the LHC radius, thus, B=8.33 T which is about 100000 times the Earth's magnetic field. A representation of the magnetic field generated by the dipole magnets is shown on the bottom left side of Figure 1.6. The bending effect of the magnetic field on the proton beam is shown on the bottom right side of Figure 1.6. Note that the dipole magnets are not curved; the arc section of the LHC ring is composed of straight dipole magnets of about 15 m. In total there are 1232 dipole magnets along the LHC ring.

In addition to the bending of the beam trajectory, the beam has to be focused. The focusing is performed by quadrupole magnets installed in a different straight section; in total 858 quadrupole magnets are installed along the LHC ring. Other effects like electromagnetic interaction among bunches, interaction with electron clouds from the beam pipe, the gravitational force on the protons, differences in energy among protons in the same bunch, among others, are corrected using sextupole and other magnetic multipoles.

The two proton beams inside the LHC ring are made of bunches with a cylindrical shape of about 7.5 cm long and about 1 mm in diameter; when bunches are close to the interaction point (IP), the beam is focused up to a diameter of about 16 μm in order to maximize the probability of collisions between protons. The number of collisions per second is proportional to the cross section of the bunches with the *luminosity* (L) as the proportionality factor, thus, the luminosity can be calculated using

$$L = fn\frac{N_1 N_2}{4\pi\sigma_x\sigma_y} \tag{1.3}$$

where f is the revolution frequency, n is the number of bunches per beam, N_1 and N_2

are the numbers of protons per bunch, σ_x and σ_y are the gaussian transverse sizes of the bunches. With the expected parameters, the LHC expected luminosity is about

$$
\begin{aligned}
f =& \frac{v}{2\pi r_{LHC}} \approx \frac{3\times 10^8 \text{m/s}}{27\text{km}} \approx 11.1\text{kHz},\\
n =& 2808\\
N_1 =& N_2 \sim 1.5\times 10^{11}\\
\sigma_x =& \sigma_y = 16\mu\text{m}
\end{aligned}
$$

$$L = 1.28\times 10^{34}\text{cm}^{-2}\text{s}^{-1} = 1.28\times 10^{-5}\text{fb}^{-1}\text{s}^{-1} \tag{1.4}$$

where 1 barn (b) corresponds to 10^{-28} m^2, hence, 1 fb $= 10^{-39}$ cm^2.

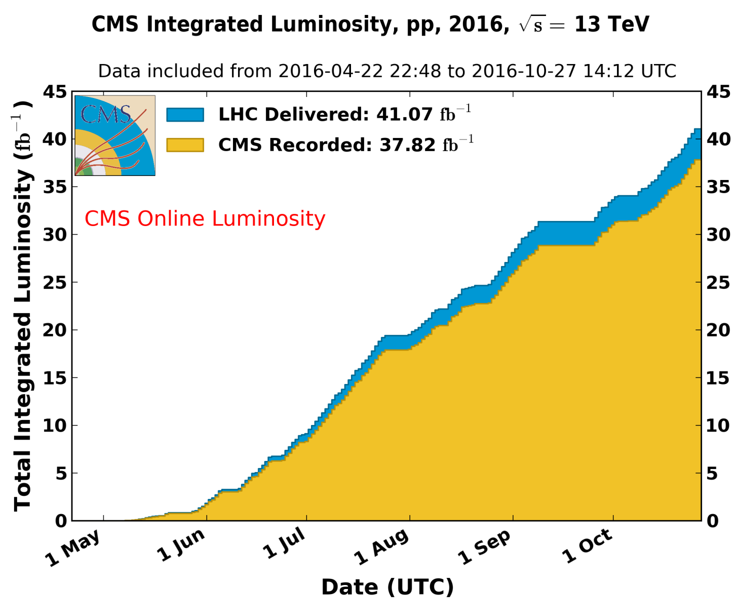

Figure 1.7: Integrated luminosity delivered by LHC and recorded by CMS during 2016. The difference between the delivered and the recorded luminosity is due to fails and issues occurred during the data taking in the CMS experiment [**?**].

Luminosity is a fundamental aspect of LHC given that the bigger luminosity the bigger number of collisions, which means that for processes with a very small cross section the number of expected occurrences is increased and so the chances of being detected. The integrated luminosity, collected by the CMS experiment during 2016 is shown in Figure 1.7; the data analyzed in this thesis corresponds to an integrated luminosity of 35.9 fb^{-1} at a center of mass-energy $\sqrt{s} = 13$ TeV.

One way to increase L is increasing the number of bunches in the beam. Currently, the separation between two consecutive bunches in the beam is 7.5 m which corresponds to a time separation of 25 ns. In the full LHC ring the allowed number of bunches is $n = 27$ km/7.5 m $= 3600$; however, there are some gaps in the bunch pattern intended for preparing the dumping and injection of the beam, thus, the proton beams are composed of 2808 bunches.

Once the proton beams reach the desired energy, they are brought to cross each other producing *pp* collisions. The bunch crossing happens in precise places where the four LHC experiments are located, as seen in the top of Figure 1.8. In 2008 *pp* collisions of $\sqrt{s} = 7$ TeV were performed; the energy was increased to 8 TeV in 2012 and to 13 TeV in 2015.

The CMS and ATLAS experiments are multi-purpose experiments, hence, they are enabled to explore physics in any of the LHC collision modes. LHCb experiment is optimized to explore bottom quark physics, while ALICE is optimized for heavy ion collisions searches; TOTEM and LHCf are dedicated to forward physics studies; MoEDAL (not indicated in the Figure) is intended for monopole or massive pseudo stable particles searches.

At the IP there are two interesting details that need to be addressed. The first one is that the bunch crossing does not occur head-on but at a small crossing angle θ_c (280 μrad in CMS and ATLAS) as shown in the bottom side of Figure 1.8, affecting the overlapping between bunches; the consequence is a reduction of about 17% in the luminosity (represented by a factor not included in eqn. 1.3). The second one

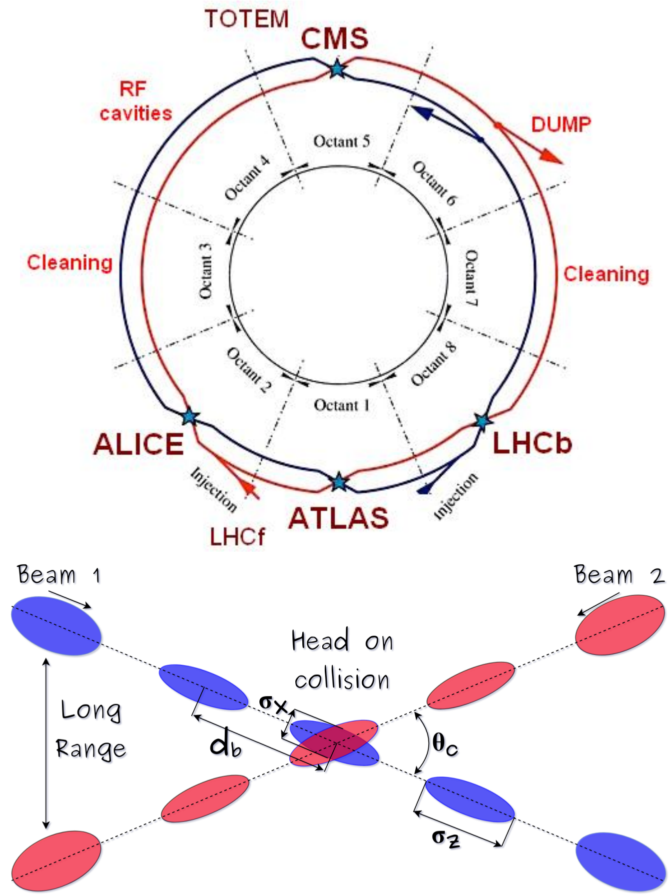

Figure 1.8: Top: LHC interaction points. Bunch crossing occurs where the LHC experiments are located [**?**]. Sections indicated as cleaning are dedicated to collimate the beam in order to protect the LHC ring from collisions with protons in very spreaded bunches. Bottom: bunch crossing scheme. Since the bunch crossing is not perfectly head-on, the luminosity is reduced in a factor of 17%; adapted from Reference [**?**].

is the occurrence of multiple *pp* collisions in the same bunch crossing; this effect is called *pileup* (PU). A fairly simple estimation of the PU follows from estimating the probability of collision between two protons, one from each of the bunches in the course of collision; it depends roughly on the ratio of proton size and the cross section of the bunch in the IP, i.e.,

$$P(pp - collision) \sim \frac{d^2_{proton}}{\sigma_x \sigma_y} = \frac{(1\text{fm})^2}{(16\mu\text{m})^2} \sim 4 \times 10^{-21} \tag{1.5}$$

however, there are $N = 1.15 \times 10^{11}$ protons in a bunch, thus the estimated number of collisions in a bunch crossing is

$$PU = N^2 * P(pp - collision) \sim 50pp \text{ collision per bunch crossing,} \tag{1.6}$$

about 20 of which are inelastic. A multiple *pp* collision event in a bunch crossing at CMS is shown in Figure 1.9.

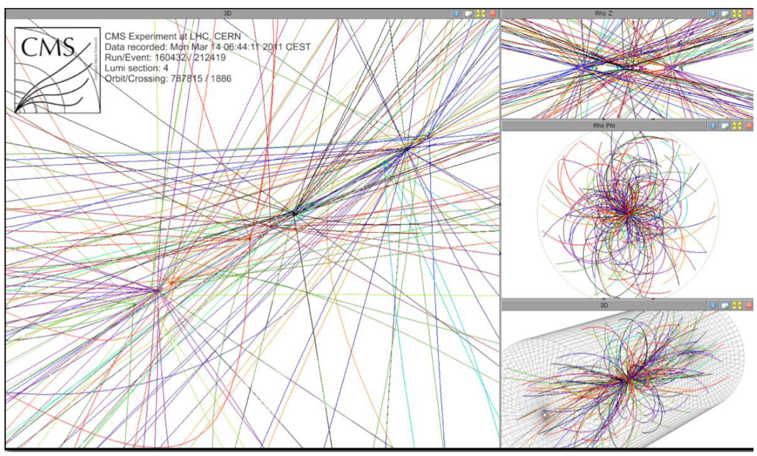

Figure 1.9: Multiple *pp* collision bunch crossing at CMS. [**?**].

1.3 The CMS experiment

CMS is a general-purpose detector designed to conduct research in a wide range of physics from the standard model to new physics like extra dimensions and dark matter. Located at Point 5 in the LHC layout as shown in Figure 1.5, CMS is composed of several detection systems distributed in a cylindrical structure; in total, CMS weights about 12500 tons in a very compact 21.6 m long and 14.6 m diameter cylinder. It was built in 15 separate sections at the ground level and lowered to the cavern individually to be assembled. A complete and detailed description of the CMS detector and its components is given in Reference [?] on which this section is based. Figure 1.10 shows the layout of the CMS detector. The detection system is composed of (from the innermost to the outermost)

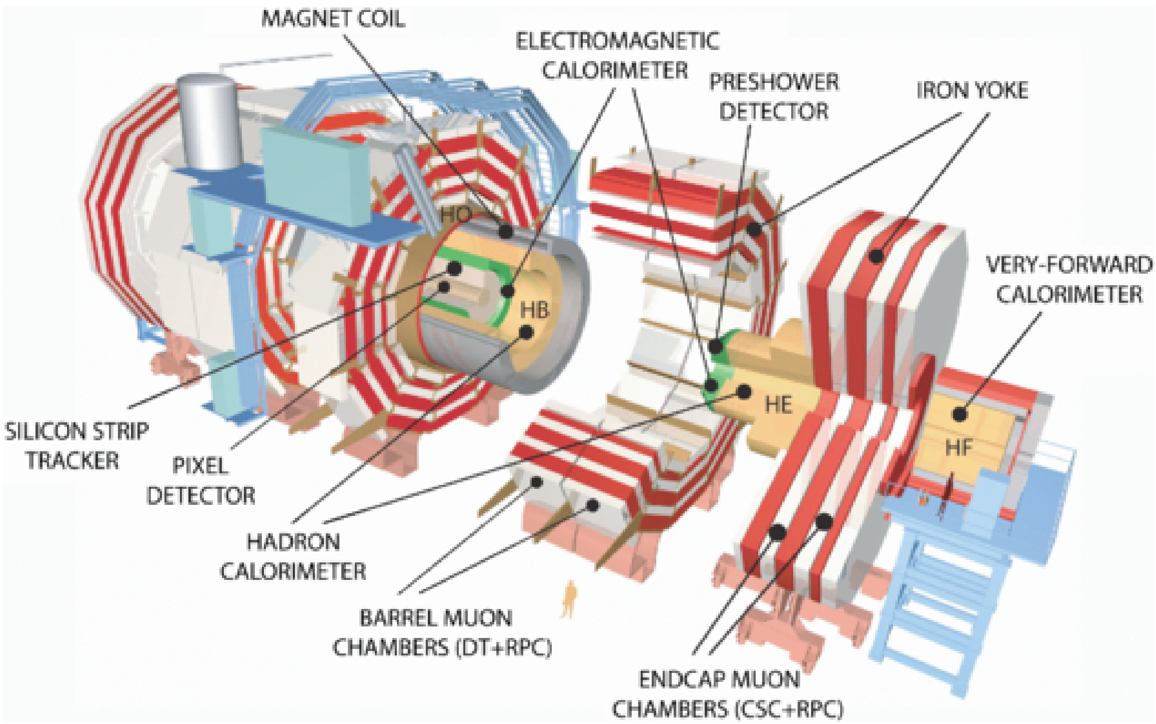

Figure 1.10: Layout of the CMS detector. The several subdetectors are indicated. The central region of the detector is referred as the barrel section while the endcaps are referred as the forward sections. [?].

- Pixel detector.
- Silicon strip tracker.
- Preshower detector.
- Electromagnetic calorimeter.
- Hadronic calorimeter.

- Muon chambers (barrel and endcap)

The central region of the detector is commonly referred as the barrel section while the endcaps are referred as the forward sections of the detector; thus, each subdetector is composed of a barrel section and a forward section.

When a *pp* collision happens inside the CMS detector, many different particles are produced, but only some of them live long enough to be detected; they are electrons, photons, pions, kaons, protons, neutrons and muons; neutrinos are not detected by the CMS detector. Thus, the CMS detector was designed to detect those particles and measure their properties. Figure 1.11 shows a transverse slice of the CMS detector. The silicon tracker (pixel detector + strip tracker) is capable to register the track of the charged particles traversing it, while calorimeters (electromagnetic and hadronic) measure the energy of the particles that are absorbed by their materials. Considering the detectable particles, mentioned above, emerging from the IP, a basic description of the detection process is as follows.

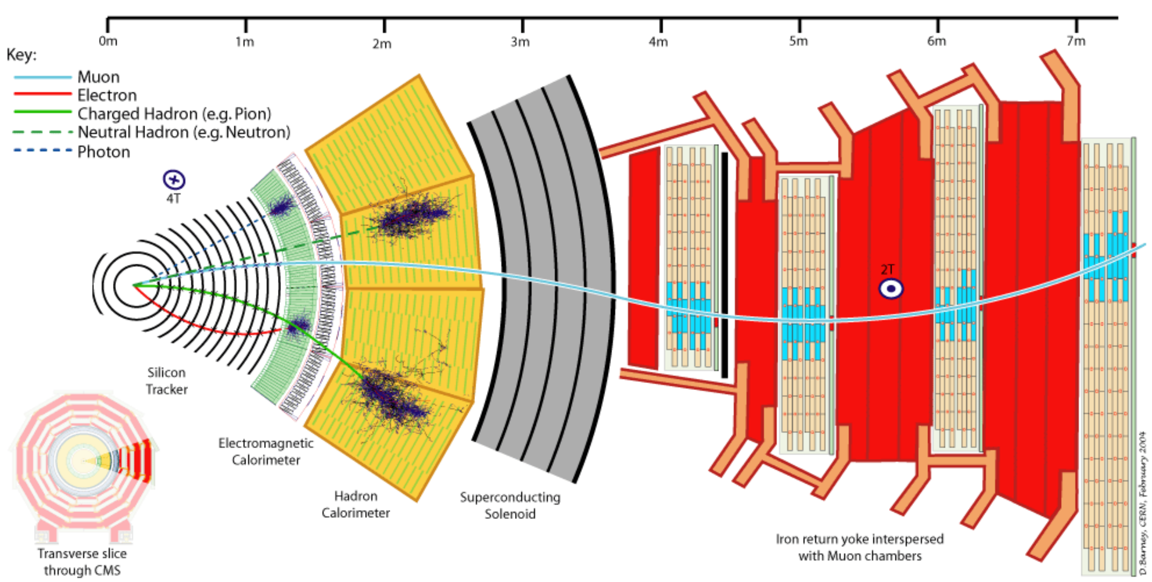

Figure 1.11: CMS detector transverse slice [?].

A muon emerging from the IP, will create a track on the silicon tracker and on the muon chambers. The design of the CMS detector is driven by the requirements on the identification, momentum resolution and unambiguous charge determination of the muons; therefore, a large bending power is provided by the solenoid magnet made of superconducting cable capable of generating a 3.8 T magnetic field. The muon track is bent twice since the magnetic field inside the solenoid is directed along the z-direction but outside its direction is reversed. Muons interact very weakly with the calorimeters, therefore, it is not absorbed but escape away from the detector.

An electron emerging from the IP will create a track along the tracker which will be bent due to the presence of the magnetic field, later, it will be absorbed in the electromagnetic calorimeter where its energy is measured.

A photon will not leave a track because it is neutral, but it will be absorbed in the electromagnetic calorimeter.

A neutral hadron, like the neutron, will not leave a track either but it will lose a small amount of its energy during its passage through the electromagnetic calorimeter and then it will be absorbed in the hadron calorimeter depositing the rest of its energy.

A charged hadron, like the proton or $\pi^{\pm}$, will leave a curved track on the silicon tracker, some of its energy in the electromagnetic calorimeter and finally will be absorbed in the hadronic calorimeter.

A more detailed description of each detection system will be presented in the following sections.

1.3.1 CMS coordinate system

The coordinate system used by CMS is centered on the geometrical center of the detector which is the nominal IP as shown in Figure 1.12[1]. The z-axis is parallel to the beam direction, while the Y-axis pointing vertically upward, and the X-axis pointing radially inward toward the center of the LHC.

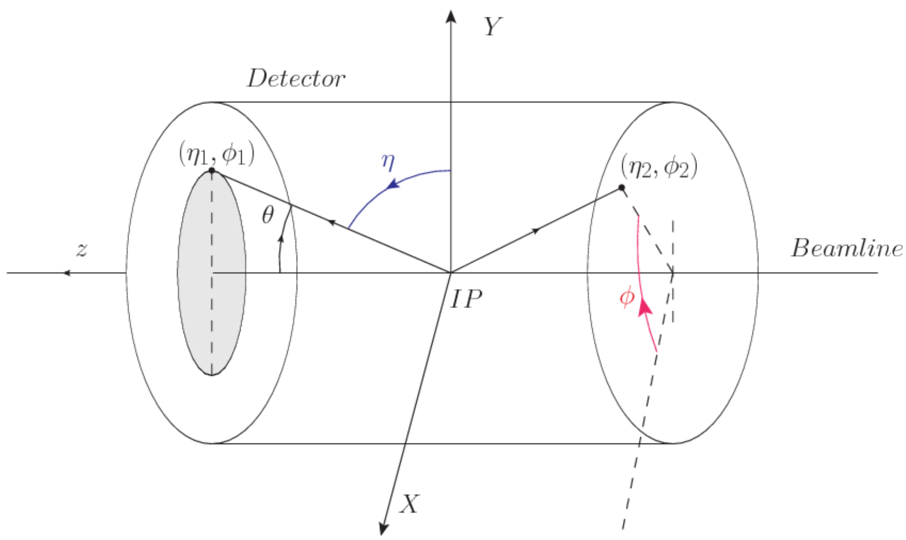

Figure 1.12: CMS detector coordinate system.

In addition to the common cartesian and cylindrical coordinate systems, two coordinates are of particular utility in particle physics: rapidity (y) and pseudorapidity (η), defined in connection to the polar angle θ, energy and longitudinal momentum component (momentum along the z-axis) according to

$$y = \frac{1}{2} ln \frac{E + p_z}{E - p_z} \qquad \eta = -ln \left(tan \frac{\theta}{2} \right) \tag{1.7}$$

Rapidity is related to the angle between the XY-plane and the direction in which the products of a collision are emitted; it has the nice property that the difference

[1] Not all the pp interaction occur at the nominal IP because of the bunch lenght, therefore, each pp collision has it own IP location

between the rapidities of two particles is invariant with respect to Lorentz boosts along the z-axis, hence, data analysis becomes more simple when based on rapidity; however, it is not simple to measure the rapidity of highly relativistic particles, as those produced after pp collisions. Under the highly relativistic motion approximation, y can be rewritten in terms of the polar angle, concluding that rapidity is approximately equal to the pseudorapidity defined above, i.e., $y \approx \eta$. Note that η is easier to measure that y given the direct relationship between the former and the polar angle.

The angular distance between two objects in the detector (ΔR) is commonly used to judge the isolation of those object; it is defined in terms of their coordinates (η_1, ϕ_1), (η_2, ϕ_2) as

$$\Delta R = \sqrt{(\Delta\eta)^2 - (\Delta\phi)^2} \tag{1.8}$$

1.3.2 Tracking system

The CMS tracking system is designed to provide a precise measurement of the trajectories (*track*) followed by the charged particles created after the pp collisions; also, the precise reconstruction of the primary and secondary origins of the tracks (*vertices*) is expected in an environment where, each 25 ns, the bunch crossing produces about 20 inelastic collisions and about 1000 particles.

Physics requirements guiding the tracking system performance include the precise characterization of events involving gauge bosons, W and Z, and their leptonic decays for which an efficient isolated lepton and photon reconstruction is of capital importance, given that isolation is required to suppress background events to a level that allows observations of interesting processes like Higgs boson decays or beyond SM events.

The ability to identify and reconstruct b-jets and B-hadrons within these jets is also a fundamental requirement, achieved through the ability to reconstruct accurately displaced vertices, given that b-jets are part of the signature of top quark physics, like the one treated in this thesis.

An schematic view of the CMS tracking system is shown in Figure 1.13

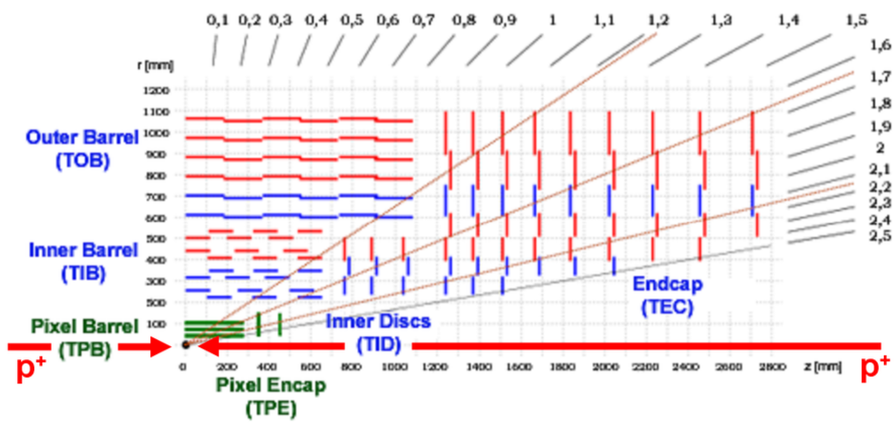

Figure 1.13: CMS tracking system schematic view [?].

In order to satisfy these performance requirements, the tracking system uses two different detector subsystems arranged in concentric cylindrical volumes, the pixel detector and the silicon strip tracker; the pixel detector is located in the high particle density region (r<20 cm) while the silicon strip tracker is located in the medium and lower particle density regions 20 cm<r<116 cm.

Pixel detector

The pixel detector was replaced during the 2016-2017 extended year-end technical stop, due to the increasingly challenging operating conditions like the higher particle flux and more radiation harsh environment, among others. The new one is responding as expected, reinforcing its crucial role in the successful way to fulfill the new LHC physics objectives after the discovery of the Higgs boson. Since the data sets used

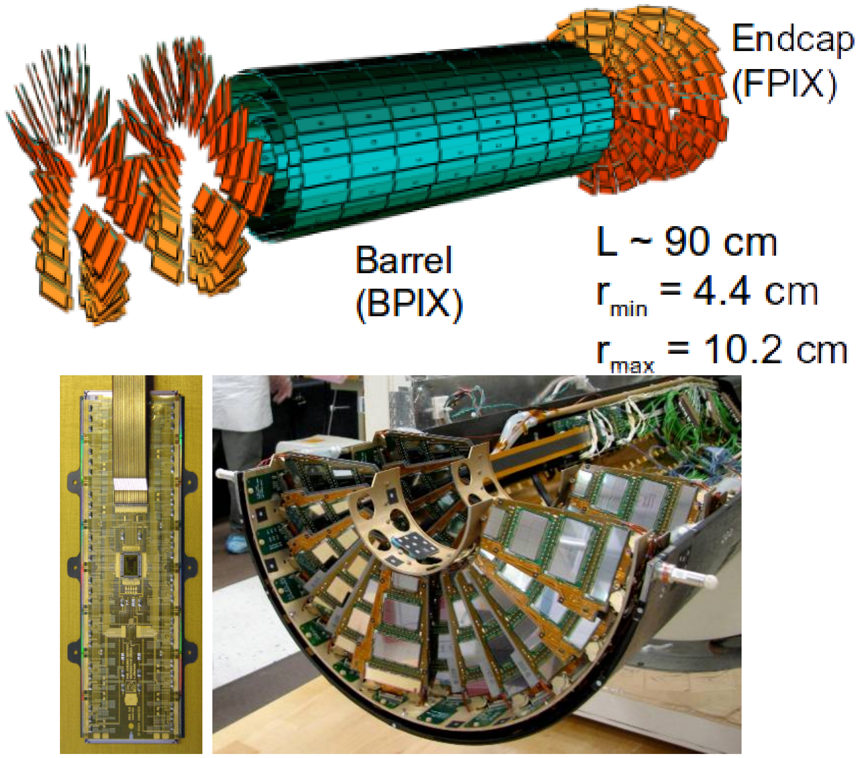

Figure 1.14: CMS pixel detector. Top: schematic view; Bottom: pictures of a barrel(BPIX) module(left) and forward modules(right) [**?**].

in this thesis were produced using the previous version of the pixel detector, it will be the subject of the description in this section. The last chapter of this thesis is dedicated to describe my contribution to the *Forward Pixel Phase 1 upgrade*.

The pixel detector was composed of 1440 silicon pixel detector modules organized in three-barrel layers in the central region (BPix) and two disks in the forward region (FPix) as shown in the top side of Figure 1.14; it was designed to record efficiently and with high precision, up to 20 μm in the XY-plane and 20 μm in the z-direction, the first three space-points (*hits*) nearest to the IP region in the range $|\eta| \leq 2.5$. The first barrel layer was located at a radius of 44 mm from the beamline, while the third layer was located at a radius of 102 mm, closer to the strip tracker inner barrel layer (see Section 1.3.3) in order to reduce the rate of fake tracks. The high granularity of the detector is represented in its about 66 Mpixels, each of size $100 \times 150\mu\text{m}^2$. The transverse momentum resolution of tracks can be measured with a resolution of 1-2% for muons of $p_T = 100$ GeV.

A charged particle passing through the pixel sensors produce ionization in them, giving energy for electrons to be removed from the silicon atoms, hence, creating electron-hole pairs. The collection of charges in the pixels generates an electrical signal that is read out by an electronic readout chip (ROC); each pixel has its own electronics which amplifies the signal. Combining the signal from the pixels activated by a traversing particle in the several layers of the detector allows one to reconstruct the particle's trajectory in 3D.

Commonly, the charge produced by traversing of a particle is collected by and shared among several pixels; by interpolating between pixels, the spatial resolution is improved. In the barrel section the charge sharing in the rϕ-plane is due to the Lorentz effect. In the forward pixels the charge sharing is enhanced by arranging the blades in the turbine-like layout as shown in Figure 1.14 bottom left.

1.3.3 Silicon strip tracker

The silicon strip tracker (SST) is the second stage in the CMS tracking system. The top side of Figure 1.15 shows a schematic of the SST. The inner tracker region is composed of the tracker inner barrel (TIB) and the tracker inner disks (TID) covering the region $r < 55$ cm and $|z| < 118$ cm. The TIB is composed of 4 layers while the TID is composed of 3 disks at each end. The silicon sensors in the inner tracker are 320 μm thick, providing a resolution of about 13-38 μm in the $r\phi$ position measurement.

The modules indicated in blue in the schematic view of Figure 1.15 are two modules mounted back-to-back and rotated in the plane of the module by a *stereo* angle

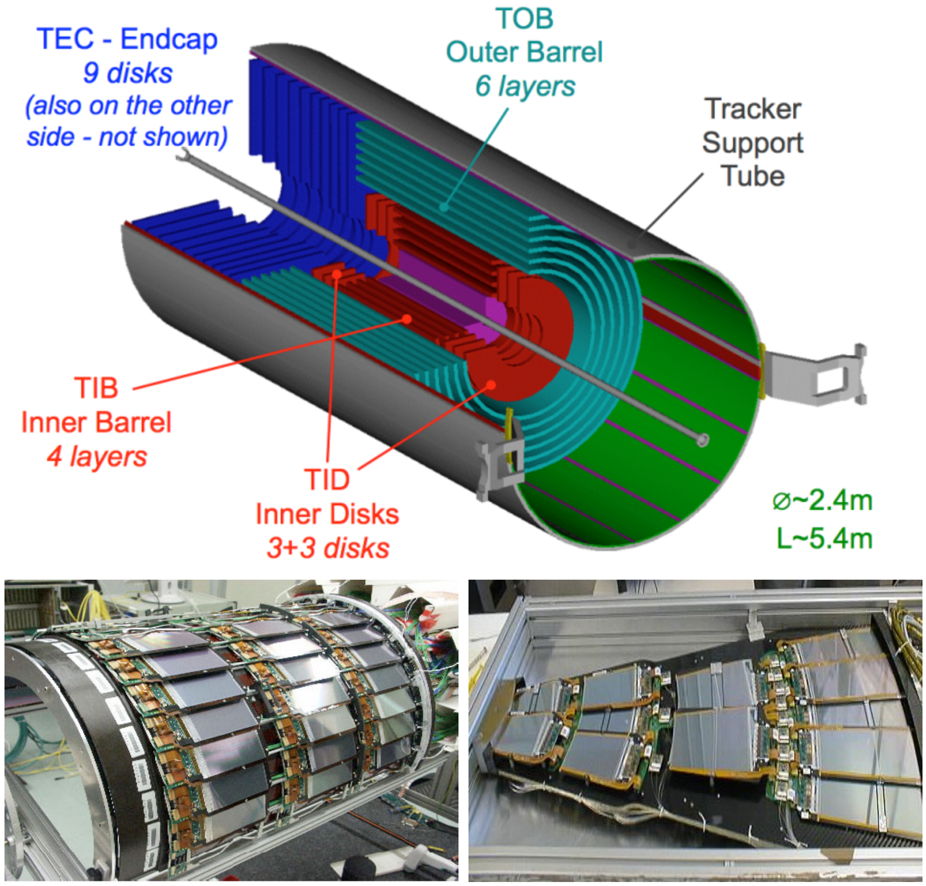

Figure 1.15: Top: CMS Silicon Strip Tracker (SST) schematic view. The SST is composed of the tracker inner barrel (TIB), the tracker inner disks (TID), the tracker outer barrel (TOB) and the tracker endcaps (TEC). Each part is made of silicon strip modules; the modules in blue represent two modules mounted back-to-back and rotated in the plane of the module by a stereo angle of 120 mrad in order to provide a 3-D reconstruction of the hit positions. Bottom: pictures of the TIB (left) and TEC (right) modules [**?**, **?**, **?**].

of 100 mrad; the hits from these two modules, known as *stereo hits*, are combined to provide a measurement of the second coordinate (z in the barrel and r on the disks) allowing the reconstruction of hit positions in 3-D.

The outer tracker region is composed of the tracker outer barrel (TOB) and the tracker endcaps (TEC). The six layers of the TOB offer coverage in the region $r > 55$ cm and $|z| < 118$ cm, while the 9 disks of the TEC cover the region $124 < |z| < 282$ cm. The resolution offered by the outer tracker is about 13-38 μm in the $r\phi$ position measurement. The inner four TEC disks use silicon sensors 320 μm thick; those in the TOB and the outer three TEC disks use silicon sensors of 500 μm thickness. The silicon strips run parallel to the z-axis and the distance between strips varies from 80 μm in the inner TIB layers to 183 μm in the inner TOB layers; in the endcaps the wedge-shaped sensors with radial strips, whose pitch range between 81 μm at small radii and 205 μm at large radii.

The whole SST has 15148 silicon modules, 9.3 million silicon strips and cover a total active area of about 198 m^2.

1.3.4 Electromagnetic calorimeter

The CMS electromagnetic calorimeter (ECAL) is designed to measure the energy of electrons and photons. It is composed of 75848 lead tungstate crystals which have a short radiation length (0.89 cm) and fast response, since 80% of the light is emitted within 25 ns; however, they are combined with Avalanche photodiodes (APDs) as photodetectors given that crystals themselves have a low light yield (30γ/MeV). A schematic view of the ECAL is shown in Figure 1.16.

Energy is measured when electrons and photons are absorbed by the crystals which generates an electromagnetic *shower*, as seen in bottom right picture of the Figure 1.16; the shower is seen as a *cluster* of energy which depending on the amount of energy deposited can involve several crystals. The ECAL barrel (EB) covers the region $|\eta| < 1.479$, using crystals of depth of 23 cm and 2.2×2.2 cm^2 transverse section; the ECAL endcap (EE) covers the region $1.479 < |\eta| < 3.0$ using crystals of depth 22 cm and transverse section of 2.86×2.86 cm^2; the photodetectors used are vacuum phototriodes (VPTs). Each EE is divided in two structures called *Dees*.

The preshower detector (ES) is installed in front of the EE and covers the region

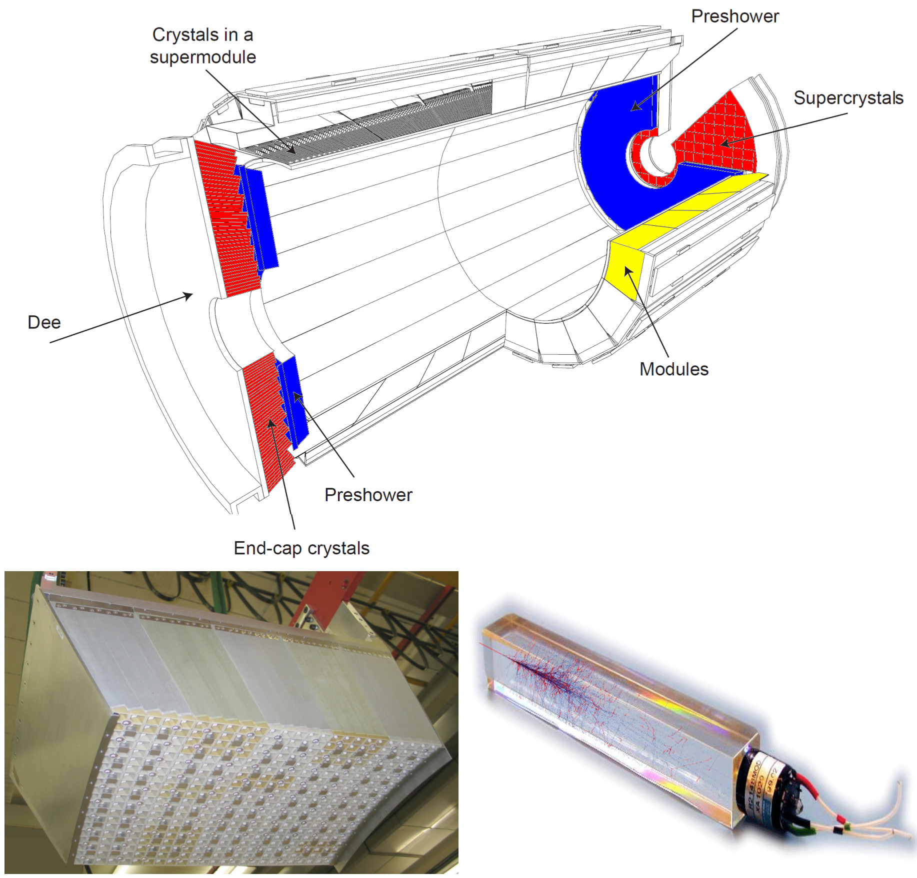

Figure 1.16: Top: CMS ECAL schematic view. Bottom: Module equipped with the crystals (left); ECAL crystal(right) with an artistic representation of an electromagnetic shower [**?**].

$1.653 < |\eta| < 2.6$. The ES provides a precise measurement of the position of electromagnetic showers, which allows to distinguish electrons and photon signals from π^0 decay signals. The ES is composed of a layer of lead radiators followed by a layer of silicon strip sensors. The lead radiators initiate electromagnetic showers when reached by photons and electrons, then, the strip sensors measure the deposited energy and the transverse shower profiles. The full ES thickness is 20 cm.

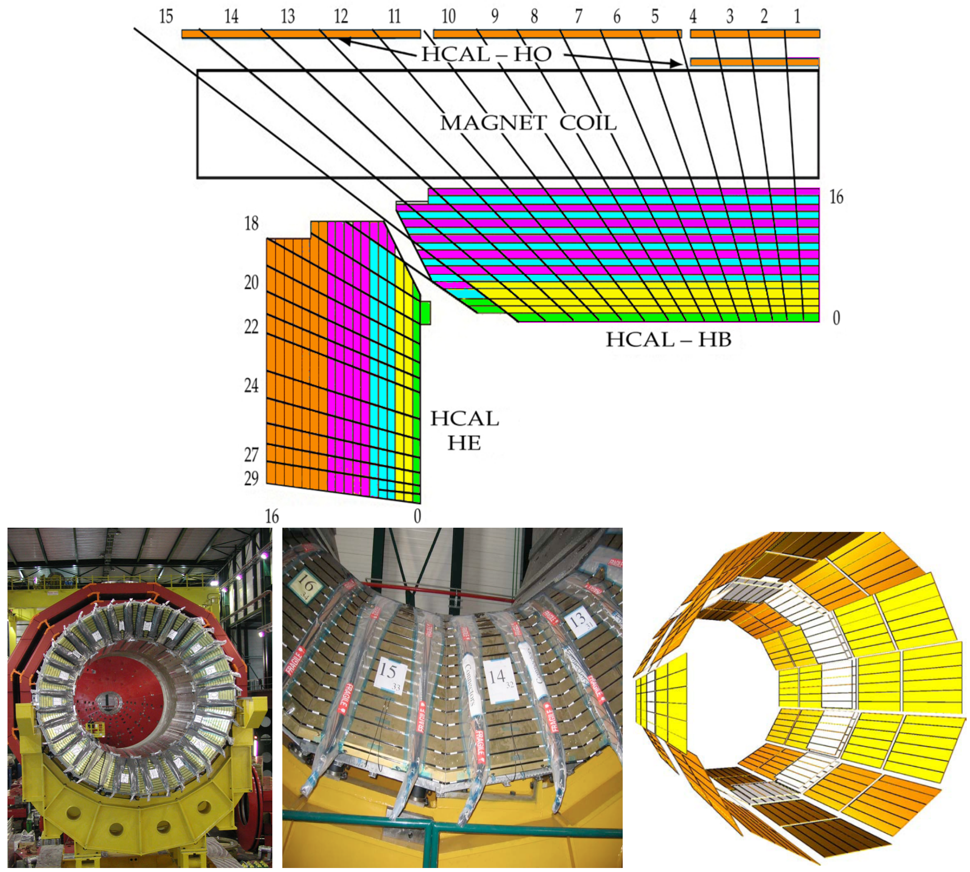

Figure 1.17: Top: CMS HCAL schematic view, the colors indicate the layers that are grouped into the same readout channels. Bottom: picture of a section of the HB; the absorber material is the golden region and scintillators are placed in between the absorber material (left and center). Schematic view of the HO (right). [**?**, **?**]

1.3.5 Hadronic calorimeter

Hadrons are not absorbed by the ECAL[2] but by the hadron calorimeter (HCAL), which is made of a combination of alternating brass absorber layers and silicon photomultiplier(SiPM) layers; therefore, particles passing through the scintillator material produce showers, as in the ECAL, as a result of the inelastic scattering of the hadrons with the detector material. Since the particles are not absorbed in the scintillator, their energy is sampled; therefore the total energy is not measured but estimated from

[2] Most hadrons are not absorbed, but few low-energy ones might be.

the energy clusters, which reduces the resolution of the detector. Brass was chosen as the absorber material due to its short interaction length ($\lambda_I = 16.42$ cm) and its non-magnetivity. Figure 1.17 shows a schematic view of the CMS HCAL.

The HCAL is divided into four sections; the Hadron Barrel (HB), the Hadron Outer (HO), the Hadron Endcap (HE) and the Hadron Forward (HF) sections. The HB covers the region $0 < |\eta| < 1.4$, while the HE covers the region $1.3 < |\eta| < 3.0$. The HF, made of quartz fiber scintillator and steel as absorption material, covers the forward region $3.0 < |\eta| < 5.2$. Both the HB and HF are located inside the solenoid. The HO is placed outside the magnet as an additional layer of scintillators with the purpose of measure the energy tails of particles passing through the HB and the magnet (see Figure 1.17 top and bottom right).

1.3.6 Superconducting solenoid magnet

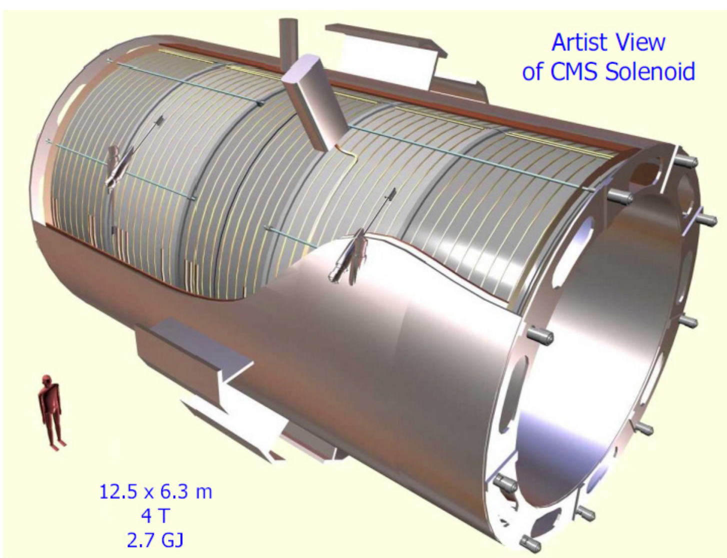

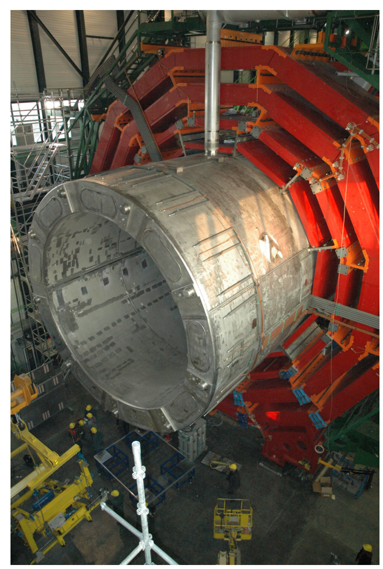

Figure 1.18: Artistic representation of the CMS solenoid magnet(left). The magnet is supported on an iron yoke (right) which also serves as the house of the muon detector and as mechanical support for the whole CMS detector [?].

The superconducting magnet installed in the CMS detector is designed to provide an intense and highly uniform magnetic field in the central part of the detector. In fact, the tracking system takes advantage of the bending power of the magnetic field to measure with precision the momentum of the particles that traverse it; the unambiguous determination of the sign for high momentum muons was a driving principle during the design of the magnet. The magnet has a diameter of 6.3 m, a length of 12.5 m and a cold mass of 220 ton; the generated magnetic field reaches a strength of 3.8T. Since it is made of Ni-Tb superconducting cable it has to operate at a temperature of 4.7 K by using a helium cryogenic system; the current circulating in the cables reaches 18800 A under normal running conditions. The left side of Figure 1.18 shows an artistic view of the CMS magnet, while the right side shows a transverse view of the cold mass where the winding structure is visible.

The yoke (see Figure 1.18), composed of 5 barrel wheels and 6 endcap disks made of iron, serves not only as the media for magnetic flux return but also provides housing for the muon detector system and structural stability to the full detector.

1.3.7 Muon system

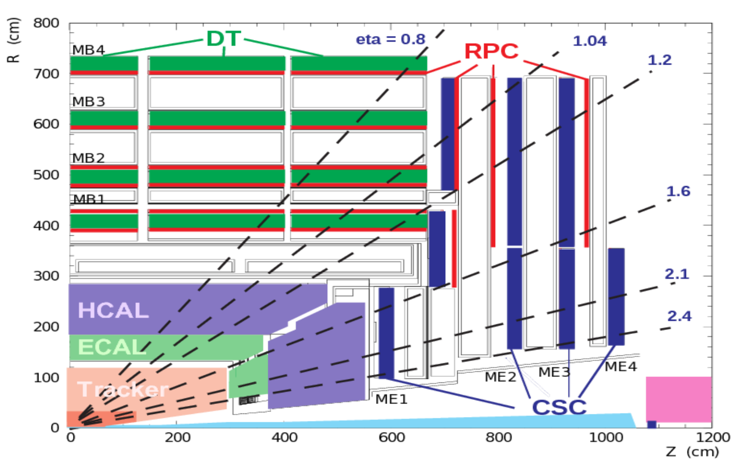

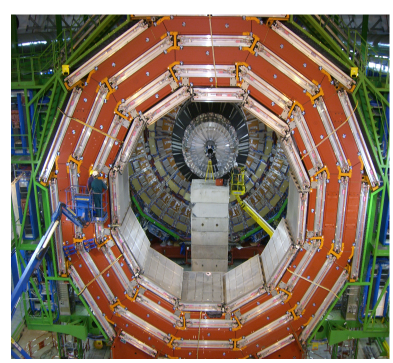

Figure 1.19: Left: CMS muon system schematic view; Right: one of the yoke rings with the muon DTs and RPCs installed; in the back it is possible to see the muon endcap [**?**].

Muons are the only charged particles able to pass through all the CMS detector due to their low ionization energy loss; thus, muons can be separated easily from the high amount of particles produced in a *pp* collision. Also, muons are expected to be produced in the decay of several new particles; therefore, good detection of muons was one of the leading principles when designing the CMS detector.

The CMS muon detection system (muon spectrometer) is embedded in the return yoke as seen in Figure 1.19. It is composed of three different detector types, the drift tube chambers (DT), cathode strip chambers (CSC), and resistive plate chambers (RPC); DT are located in the central region $\eta < 1.2$ arranged in four layers of drift chambers filled with an Ar/CO_2 gas mixture.

The muon endcaps are made of CSCs covering the region $\eta < 2.4$ and filled with a mixture of $Ar/CO_2/CF_4$. The reason behind using a different detector type lies on the different conditions in the forward region like the higher muon rate and higher residual magnetic field compared to the central region.

The third type of detector used in the muon system is a set of four disks of RPCs working in avalanche mode. The RPCs provide good spatial and time resolutions. The track of high-p_T muon candidates is built combining information from the tracking system and the signal from up to six RPCs and four DT chambers.

The muon tracks are reconstructed from the hits in the several layers of the muon system.

1.3.8 CMS trigger system

CMS expects *pp* collisions every 25 ns, i.e., an interaction rate of 40 MHz for which it is not possible to store the recorded data in full. In order to handle this high event rate data, an online event selection, known as triggering, is performed; triggering reduces the event rate to 100 Hz for storage and further offline analysis.

The trigger system starts with a reduction of the event rate to 100 kHz in the so-called *the level 1 trigger* (L1). L1 is based on dedicated programmable hardware like Field Programmable Gate Arrays (FPGAs) and Application Specific Integrated Circuits (ASICs), partly located in the detector itself; another portion is located in the CMS underground cavern. Hit pattern information from the muon chambers and the energy deposits in the calorimeter are used to decide if an event is accepted or rejected, according to selection requirements previously defined, which reflect the interesting physics processes. Figure 1.20 shows the L1 trigger architecture.

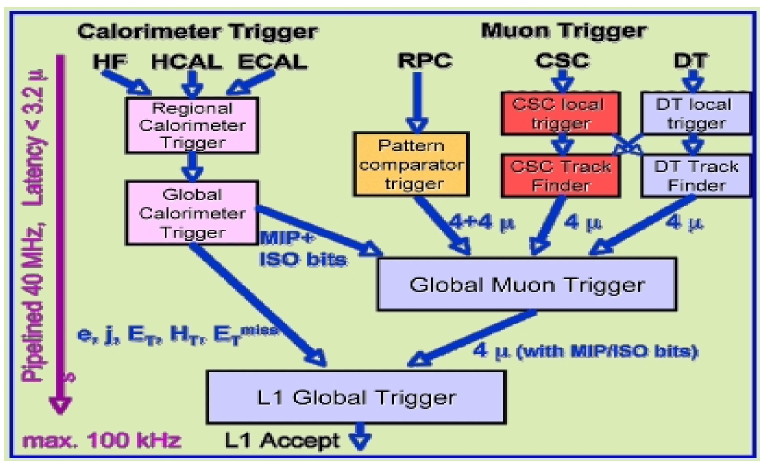

Figure 1.20: CMS Level-1 trigger architecture [**?**].

The second stage in the trigger system is called *the high-level trigger* (HLT); events accepted by L1 are passed to HLT in order to make an initial reconstruction of them. HLT is software based and runs on a dedicated server farm, using selection algorithms and high-level object definitions; the event rate at HLT is reduced to 100 Hz. The first HLT stage takes information from the muon detectors and the calorimeters to make the initial object reconstruction; in the next HLT stage, information from the pixel and strip detectors is used to do first fast tracking and then full tracking online. This initial object reconstruction is used in further steps of the trigger system.

Events and preliminary reconstructed physics objects from HLT are sent to be fully reconstructed at the CERN computing center know also as Tier-0 facility. Again, the pixel detector information provides high-quality seeds for the track reconstruction algorithm offline, primary vertex reconstruction, electron and photon identification, muon reconstruction, τ identification, and b-tagging. After full reconstruction, data sets are made available for offline analyses.

Sometimes, a trigger *prescale* is introduced in order to reduce even further the event rate; thus, for a prescaling of ten only one of each ten events passing the trigger requirements is saved.

1.3.9 CMS computing

Data coming from the experiment have to be stored and made available for further analysis; in order to cope with all the tasks implied in the offline data processing, like transfer, simulation, reconstruction and reprocessing, among others, a large computing power is required. The CMS computing system is based on the distributed architecture concept, where users of the system and physical computer centers are distributed worldwide and interconnected by high-speed networks.

The worldwide LHC computing grid (WLCG) is the mechanism used to provide that distributed environment. WLCG is a tiered structure connecting computing centers around the world, which provides the necessary storage and computing facilities. The primary computing centers of the WLCG are located at the CERN and the Wigner datacenter in Budapest and are known as Tier-0 as shown in Figure 1.21. The main responsibilities for each tier level are [**?**]

- **Tier-0**: initial reconstruction of recorded events and storage of the resulting datasets, the distribution of raw data to the Tier-1 centers.

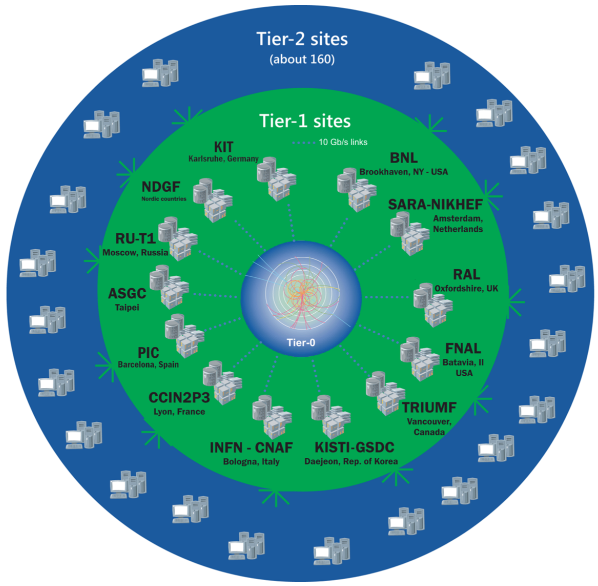

Figure 1.21: WLCG structure. The primary computer centers (Tier-0) are located at CERN (data center) and at the Wigner datacenter in Budapest. Tier-1 is composed of 13 centers and Tier-2 is composed of about 160 centers. [**?**].

- **Tier-1**: provide storage capacity, support for the Grid, safe-keeping of a proportional share of raw and reconstructed data, large-scale reprocessing and safe-keeping of corresponding output, generation of simulated events, distribution of data to Tier 2s, safe-keeping of a share of simulated data produced at these Tier 2s.

- **Tier-2**: store sufficient data and provide adequate computing power for specific analysis tasks and proportional share of simulated event production and reconstruction.

Aside from the general computing strategy to manage the huge amount of data produced by experiments, CMS uses a software framework to perform a variety of processing, selection and analysis tasks. The central concept of the CMS data model referred to as *event data model* (EDM) is the *Event*; therefore, an event is the unit that contains the information from a single bunch crossing, any data derived from that information like the reconstructed objects, and the details of the derivaction.

Events are passed as the input to the *physics modules* that obtain information from them and create new information; for instance, *event data producers* add new data into the events, *analyzers* produce an information summary from an event set, *filters* perform selection and triggering.

CMS uses several event formats with different levels of detail and precision

- **Raw format**: events in this format contain the full recorded information from the detector as well as trigger decision and other metadata. An extended version of raw data is used to store information from the CMS Monte Carlo simulation tools (see Chapter **??**). Raw data are stored permanently, occupying about 2MB/event

- **RECO format**: events in this format correspond to raw data that have been submitted to reconstruction algorithms like primary and secondary vertex reconstruction, particle ID, and track finding. RECO events contain physics objects and all the information used to reconstruct them; average size is about 0.5 MB/event.

- **AOD format**: Analysis Object Data (AOD) is the data format used in the physics analyses given that it contains the parameters describing the high-level physics objects in addition to enough information to allow a kinematic refitting if needed. AOD events are filtered versions of the RECO events to which skimming or other filtering have been applied, hence AOD events are subsets of RECO events. Requires about 100 kB/event.

- **Non-event data** are data needed to interpret and reconstruct events. Some of the non-event data used by CMS contains information about the detector contraction and condition data like calibrations, alignment, and detector status.

Figure 1.22 shows the data flow scheme between CMS detector and tiers.

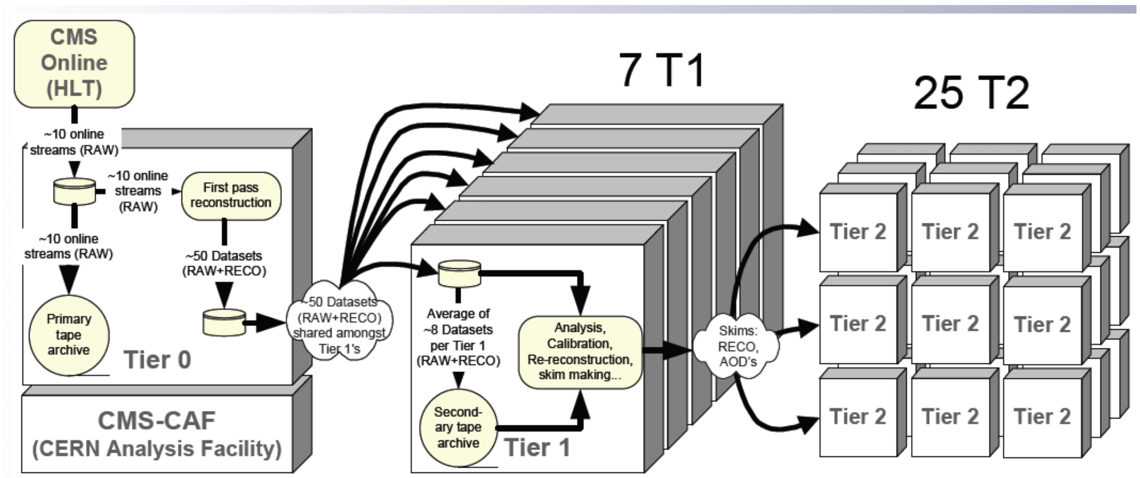

Figure 1.22: Data flow from CMS detector through tiers.

The whole collection of software built as a framework is referred to as *CMSSW*. This framework provides the services needed by the simulation, calibration and alignment, and reconstruction modules that process event data, so that physicists can perform analysis. The CMSSW event processing model is composed of one executable, called cmsRun, and several plug-in modules which contains all the tools (calibration, reconstruction algorithms) needed to process an event. The same executable is used for both detector data and Monte Carlo simulations [**?**].

References

[1] Matthias U. Mozer. Electroweak Physics at the LHC. *Springer Tracts Mod. Phys.*, 267:1–115, 2016.

[2] Gennadi Sardanashvily. *Noether's theorems: applications in mechanics and field theory*. Atlantis studies in variational geometry. Springer, Paris, 2016.

[3] Steven Weinberg. The Making of the Standard Model. *Eur. Phys. J. C*, 34(hep-ph/0401010):5–13. 21 p. ; streaming video, 2003.

[4] Roger Wolf. *The Higgs Boson Discovery at the Large Hadron Collider*, volume 264. Springer, 2015.

[5] Jose Andres Monroy Montanez, Kenneth Bloom, and Aaron Dominguez. Search for production of a Higgs boson and a single Top quark in multilepton final states in pp collisions at $\sqrt{s} = 13$ TeV, Jul 2018. Presented 23 Jul 2018.

[6] Peisi Huang, Aniket Joglekar, Min Li, and Carlos E. M. Wagner. Corrections to di-Higgs boson production with light stops and modified Higgs couplings. *Phys. Rev.*, D97(7):075001, 2018.

[7] Matthew J. Dolan, Christoph Englert, and Michael Spannowsky. New Physics in LHC Higgs boson pair production. *Phys. Rev.*, D87(5):055002, 2013.

[8] Shinya Kanemura, Kunio Kaneta, Naoki Machida, Shinya Odori, and Tetsuo Shindou. Single and double production of the Higgs boson at hadron and lepton colliders in minimal composite Higgs models. *Phys. Rev.*, D94(1):015028, 2016.

[9] Albert M Sirunyan et al. Search for Higgs boson pair production in the $\gamma\gamma\mathrm{b}\overline{\mathrm{b}}$ final state in pp collisions at $\sqrt{s} = 13$ TeV. 2018.

[10] Alexandra Oliveira. Gravity particles from Warped Extra Dimensions, predictions for LHC. 2014.

[11] Lisa Randall and Raman Sundrum. A Large mass hierarchy from a small extra dimension. *Phys. Rev. Lett.*, 83:3370–3373, 1999.

[12] Kunihito Uzawa, Yoshiyuki Morisawa, and Shinji Mukohyama. Excitation of Kaluza-Klein gravitational mode. *Phys. Rev.*, D62:064011, 2000.

[13] H. Davoudiasl, J. L. Hewett, and T. G. Rizzo. Phenomenology of the Randall-Sundrum Gauge Hierarchy Model. *Phys. Rev. Lett.*, 84:2080, 2000.

[14] Michael Forger and Hartmann Romer. Currents and the energy momentum tensor in classical field theory: A Fresh look at an old problem. *Annals Phys.*, 309:306–389, 2004.

[15] Chuan-Ren Chen and Ian Low. Double take on new physics in double Higgs boson production. *Phys. Rev.*, D90(1):013018, 2014.

[16] Roberto Contino, Margherita Ghezzi, Mauro Moretti, Giuliano Panico, Fulvio Piccinini, and Andrea Wulzer. Anomalous Couplings in Double Higgs Production. *JHEP*, 08:154, 2012.

[17] Richard Phillips Feynman, Robert Benjamin Leighton, and Matthew Sands. *The Feynman lectures on physics; New millennium ed.* Basic Books, New York, NY, 2010. Originally published 1963-1965.

[18] Savas Dimopoulos, Stuart Raby, and Frank Wilczek. Proton decay in supersymmetric models. *Physics Letters B*, 112(2):133 – 136, 1982.

[19] David J Griffiths. *Introduction to elementary particles; 2nd rev. version.* Physics textbook. Wiley, New York, NY, 2008.

[20] M. Della Negra, P. Jenni, and T. S. Virdee. Journey in the search for the higgs boson: The atlas and cms experiments at the large hadron collider. *Science*, 338(6114):1560–1568, 2012.

[21] Jennifer Ouellette. Einstein's quest for a unified theory. *APS*, 2015.

[22] E A Davis and Isabel Falconer. *J.J. Thompson and the discovery of the electron.* Taylor and Francis, Hoboken, NJ, 2002.

[23] Oreste Piccioni. *The Discovery of the Muon*, pages 143–162. Springer US, Boston, MA, 1996.

[24] G. Danby, J-M. Gaillard, K. Goulianos, L. M. Lederman, N. Mistry, M. Schwartz, and J. Steinberger. Observation of high-energy neutrino reactions and the existence of two kinds of neutrinos. *Phys. Rev. Lett.*, 9:36–44, Jul 1962.

[25] M. L. Perl, G. S. Abrams, and et al Boyarski. Evidence for anomalous lepton production in $e^+ - e^-$ annihilation. *Phys. Rev. Lett.*, 35:1489–1492, Dec 1975.

[26] K. Kodama et al. Observation of tau neutrino interactions. *Phys. Lett.*, B504:218–224, 2001.

[27] S. M. Bilenky. Neutrino in Standard Model and beyond. *Phys. Part. Nucl.*, 46(4):475–496, 2015.

[28] S Chandrasekhar. *Newton's principia for the common reader.* Oxford Univ., Oxford, 2003. The book can be consulted by contacting: PH-AID: Wallet, Lionel.

[29] Hanoch Gutfreund and Jürgen Renn. *The road to relativity: the history and meaning of Einstein's "The foundation of general relativity" : featuring the original manuscript of Einstein's masterpiece.* Princeton University Press, Princeton, NJ, Apr 2015.

[30] J. Butterworth. *Smashing Physics.* Headline Publishing Group, 2014.

[31] W N Cottingham and D A Greenwood. *An Introduction to the Standard Model of Particle Physics; 2nd ed.* Cambridge Univ. Press, Cambridge, 2007.

[32] Eric W. Weisstein. Fundamental forces.

[33] Carl Bender. Mathematical physics.

[34] Andrew Wayne. QED and the Men Who Made It: Dyson, Feynman, Schwinger, and Tomonaga by Silvan S. Schweber. *The British Journal for the Philosophy of Science*, 46(4):624–627, 1995.

[35] C. Patrignani et al. Review of Particle Physics. *Chin. Phys.*, C40(10):100001, 2016.

[36] Michelangelo L Mangano. Introduction to QCD. (CERN-OPEN-2000-255), 1999.

[37] Matt Strassler. Of particular significance: Conversations about science with theoretical physicist matt strassler.

[38] S. L. Glashow. Partial Symmetries of Weak Interactions. *Nucl. Phys.*, 22:579–588, 1961.

[39] F. Englert and R. Brout. Broken symmetry and the mass of gauge vector mesons. *Phys. Rev. Lett.*, 13:321–323, Aug 1964.

[40] Peter W. Higgs. Broken symmetries and the masses of gauge bosons. *Phys. Rev. Lett.*, 13:508–509, Oct 1964.

[41] G. S. Guralnik, C. R. Hagen, and T. W. B. Kibble. Global conservation laws and massless particles. *Phys. Rev. Lett.*, 13:585–587, Nov 1964.

[42] Pauline Gagnon. *Who cares about particle physics? : making sense of the Higgs boson, the Large Hadron Collider and CERN.* Oxford University Press, 2016.